Journal of Materials Chemistry A

PAPER

View Article Online
View Journal | View Issue

Cite this: J. Mater. Chem. A, 2016, 4, 10329

All-solid-state lithium-ion batteries with TiS_2 nanosheets and sulphide solid electrolytes†

Dae Yang Oh,[a] Young Eun Choi,[a] Dong Hyeon Kim,[a] Young-Gi Lee,[b] Byeong-Su Kim,[c] Jongnam Park,[a] Hiesang Sohn[d] and Yoon Seok Jung*[a]

Received 24th February 2016
Accepted 4th June 2016

DOI: 10.1039/c6ta01628f

www.rsc.org/MaterialsA

Bulk-type all-solid-state lithium-ion batteries (ASLBs) using sulphide solid electrolytes (SEs) are considered as one of the promising alternative batteries because of their ultimate safety and scalable fabrication. However, they suffer from poor ionic contacts between active materials and SEs. Herein, we report, for the first time, the excellent electrochemical performances of sulphide-SE-based bulk-type ASLBs employing TiS_2 nanosheets (TiS_2-NSs) prepared by scalable mechanochemical lithiation, followed by exfoliation in water under ultrasonication. The TiS_2-NS in all-solid-state cells exhibits an enhancement of reversible capacity which is attributed to the SE region in intimate contact with TiS_2-NSs. Importantly, an exceptionally superior rate capability of the TiS_2-NS compared to that of bulk TiS_2 and even ball-milled TiS_2, which is attributed to the ultrathin 2D structure (with short Li-ion diffusion length and intimate contacts between the TiS_2-NS and SE) and high electronic conductivity, is highlighted.

Introduction

Large-scale energy storage applications such as in electric vehicles and smart grids require unprecedentedly strict safety features (*e.g.*, non-flammability and no leakage). As a means of meeting this demand, all-solid-state lithium batteries (ASLBs), in which the conventional organic liquid electrolyte solution is substituted by inorganic solid electrolytes (SEs), have attracted much attention.[1–6] In particular, bulk-type ASLBs in which composite-structured electrodes are fabricated from the particulate mixtures of active materials, SE powders, and conductive additives are considered as competitors for conventional lithium-ion batteries (LIBs) in terms of scalable production and energy density.[1–6] Among the various SE materials, superionic sulphide SEs are strong candidates for application in bulk-type ASLBs.[1,7] High ionic conductivity rivalling that of organic liquid electrolytes (~10 mS cm^{-1}) has been achieved with several sulphide materials (*e.g.*, $Li_{10}GeP_2S_{12}$ (LGPS, 12 mS cm^{-1}) and $Li_7P_3S_{11}$ (17 mS cm^{-1})).[1,7,8] Furthermore, the softness of sulphide SE materials makes it possible to form 2-dimensional (2D) contacts with active materials by simple cold-pressing[2,3,9,10] without the requirement for the high-temperature sintering process that is necessary for ASLBs employing brittle oxide SEs.[2,11,12]

However, one of the most critical drawbacks of sulphide SEs is their poor compatibility with conventional transition metal oxide cathode materials such as $LiCoO_2$.[13–17] Large interfacial resistance is observed when $LiCoO_2$ is used in contact with sulphide SEs.[13,14,17] This resistance is explained by the interfacial chemical reaction (which is evidenced by interatomic diffusion),[18] the space-charge layer mechanism,[13] poor stability of the sulphide SE at high voltage (>3 V *vs.* Li/Li^+),[15] and possible lattice mismatch.[19] The surface protection of $LiCoO_2$ by using various oxide materials (*e.g.*, $LiNbO_3$,[1] $Li_4Ti_5O_{12}$,[13] Al_2O_3,[16] and Ta_2O_5 [20]) has been applied to achieve improved electrochemical performance. Alternatively, transition metal sulphides can be employed as a means of circumventing the undesirable poor interface between oxide cathode materials and sulphide SEs. Better sulphide–sulphide compatibility and mild operating voltages are potentially advantageous for sulphide cathode materials.[21,22] Previously, our group presented TiS_2-based electrodes for bulk-type ASLBs.[10,15,21] The promising performance of the TiS_2-based ASLBs was attributed to the architecture featuring synergism between the metallic conductivity and ductility of TiS_2, in conjunction with the favourable contacts between TiS_2 and the SEs.[15,21]

In this context, 2D nanosheets (NSs) of sulphide materials represent promising electrode materials for bulk-type ASLBs employing sulphide SEs because more intimate contact with the SEs may be possible. Single nanosheets and few-layer nanosheets of transition metal dichalcogenides (TMDs) have

[a]School of Energy and Chemical Engineering, Department of Energy Engineering, Ulsan National Institute of Science and Technology (UNIST), Ulsan 44919, South Korea. E-mail: ysjung@unist.ac.kr

[b]Power Control Device Research Team, Electronics and Telecommunications Research Institute (ETRI), 218, Gajeongno, Yuseong-gu, Daejeon, 305-700, South Korea

[c]Department of Chemistry, Department of Energy Engineering, Ulsan National Institute of Science and Technology (UNIST), Ulsan 44919, South Korea

[d]The Pennsylvania State University, Department of Mechanical and Nuclear Engineering, University Park, PA, 16802, USA

† Electronic supplementary information (ESI) available. See DOI: 10.1039/c6ta01628f

provided new opportunities for fundamental studies as well as a variety of applications for electronic devices, sensors, catalysts, and batteries because of their unique properties.[23,24] The ultrathin morphology enabled significantly improved performance during the application of exfoliated NSs of TMDs to batteries.[25–27] Lemmon *et al.* reported that exfoliated MoS_2 composited with polyethylene oxide exhibited an initial discharge capacity of >1000 mA h g^{-1} between 0.01 and 3.00 V at 50 mA g^{-1}, in contrast with the low capacity of <300 mA h g^{-1} of pristine MoS_2.[25] Despite the availability of NSs of various TMD materials (*e.g.*, MoS_2, WS_2, TiS_2, TaS_2, and NbS_2),[23,24] studies on the application of TMD NSs to batteries have been limited mostly to MoS_2.[25–27] Notably, the metallic conductivity[15,21] of TiS_2 and the reversibility of its reaction with Li[15,21,28] make TiS_2 a promising candidate for exploration of the performance of its exfoliated NS form in batteries, which has not yet been evaluated. However, the scalability of the synthesis protocols for generating exfoliated TMD NSs remains an obstacle for their practical application in batteries. The methods for lithiation of TMDs include the wet chemical reaction and electrochemical reaction, which are time-consuming and tedious, making scale-up difficult.[23,24,29–31] For example, the wet chemical lithiation method using *n*-butyllithium is expensive and has a risk of explosion.[23,24,29]

Based on the aforediscussed background and motivation, herein, we report, for the first time, the excellent performance of sulphide-SE-based bulk-type ASLBs employing TiS_2 NSs. The TiS_2 NSs are prepared by scalable mechanochemical lithiation, followed by exfoliation in water under ultrasonication. The composite electrode tailored with the TiS_2 NSs exhibits enhanced capacity, significantly enhanced rate capability and cycling performance, illustrating the potential of these electrodes.

Experimental

Preparation of materials

The protocol for the preparation of TiS_2 nanosheets (TiS_2-NSs) is illustrated in Fig. 1. Lithiated TiS_2 (LTS) powders were prepared by mechanical milling. 250 mg of a mixture of Li_3N (33.7 mg, Alfa Aesar, 99.4%) and TiS_2 (216.3 mg, Sigma Aldrich, 99.9%) was mechanically milled at 500 rpm for 2 h at room temperature with a steel vial (80 mL) and 5 ZrO_2 balls (5 mm in diameter). TiS_2-NSs were prepared by liquid-phase exfoliation of the as-prepared LTS powders. 80 mg of LTS powders were dispersed in 120 mL of deoxygenated and deionized water, which was followed by ultrasonication at 50% power amplitude for 1 h at room temperature using VCX 750 (Sonic & Materials Co.). The TiS_2-NS powders were then collected by centrifuging the solution several times at 3000 rpm and subsequent drying under vacuum at 150 °C overnight. In all the procedures, exposure to ambient air was avoided by sealing the samples under Ar.

LPS SE powders were prepared by a mechanical milling process which is followed by heat treatment at a temperature above the crystallization temperature.[21] 2 g of a stoichiometric mixture of Li_2S (99.9%, Alfa Aesar) and P_2S_5 (99%, Sigma Aldrich) powders were mechanically milled at 500 rpm for 10 h at room temperature using a Pulverisette with a zirconia vial (80 mL) and 115 g of zirconia balls. The obtained glass powders were sealed in a glass ampoule under vacuum and heat treated at 244 °C for 1 h. $Li_{10}GeP_2S_{12}$ (LGPS) SE powders were prepared by the solid-state reaction of a stoichiometric mixture of Li_2S (99.9%, Alfa Aesar), P_2S_5 (99%, Sigma Aldrich), and GeS_2 (99.9%, American Elements) powders in a sealed glass ampoule at 550 °C for 12 h.[15]

All-solid-state cells

The composite electrodes consist of active materials, SE, and carbon additives as conducting agents. The mixture of active materials (b-TiS_2 or TiS_2-NS), LGPS powders, and Super P (10 : 10 : 0.5 wt ratio) was manually prepared. Partially lithiated indium ($Li_{0.5}In$, nominal composition) powders were prepared by mechanically milling the mixture of In (Sigma Aldrich, 99.99%) and Li (FMC Lithium corp.). In order to fabricate the all-solid-state cells, the LGPS/LPS SE bi-layer film was formed by pelletizing 120 mg of LGPS and 30 mg of LPS under 72 MPa. 10 mg of the as-prepared electrode mixture was spread on the side of LGPS and pressed under 370 MPa. Then, 100 mg of the $Li_{0.5}In$ powders were laid on the side of LPS and pressed under 370 MPa. All the pressing was carried out in a polyaryletheretherketone (PEEK) mold (diameter = 13 mm) with Ti rods as current collectors. The galvanostatic discharge–charge cycling of the all-solid-state cells was

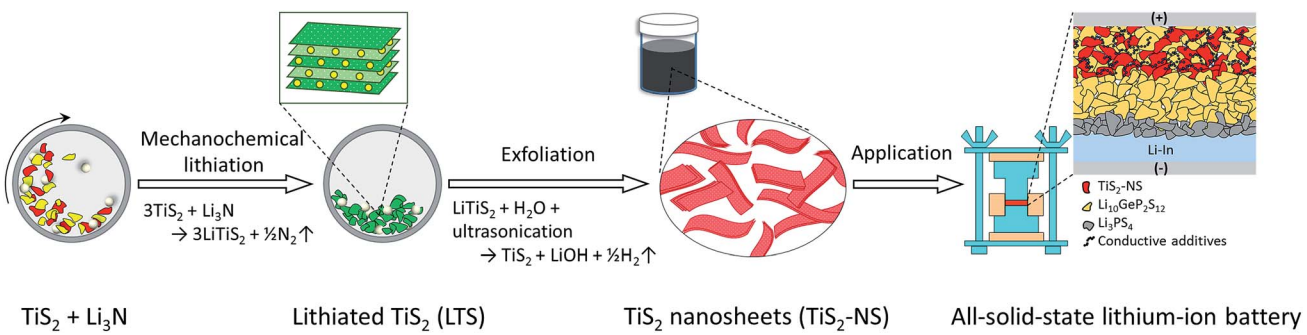

Fig. 1 Schematic diagram illustrating the preparation of TiS_2 nanosheets (TiS_2-NSs) and their application in bulk-type all-solid-state lithium-ion batteries (ASLBs) using sulphide SEs.

performed in the voltage range of 1.0–4.0 V (*vs.* Li/Li^+) at 30 °C. The capacity is based on the weight of active materials (TiS_2).

Liquid-electrolyte cell

The cycling tests using liquid electrolytes were carried out by using 2032-type coin cells. The composite electrodes were prepared by spreading TiS_2-NS, Super P, and a poly(vinylidene fluoride) (PVDF) binder (KF1100, Kureha Inc.) on Al foil. The weight ratio of TiS_2-NS : Super P : PVDF was 70 : 15 : 15. The electrode was prepared inside an Ar-filled dry box. Li metal foil was used as both counter and reference electrodes. A 1.0 M solution of $LiPF_6$ dissolved in a mixture of ethylene carbonate (EC), ethylmethyl carbonate (EMC), and dimethyl carbonate (DMC) (3 : 4 : 3 v/v) was used as the electrolyte. 2032-type coin cells were assembled in an Ar-filled dry glove box. Galvanostatic charge–discharge cycling was carried out between 1.0 and 4.0 V (*vs.* Li/Li^+) at 50 mA g^{-1} at 30 °C.

Materials characterization

For XRD analyses, a specially designed XRD cell was used. The samples were placed on a beryllium window and hermetically sealed inside an Ar-filled dry box, and mounted on a D8-Bruker Advance diffractometer (Cu K_α radiation is 1.54056 Å). The XRD data were recorded at 40 kV and 40 mA at 15° min^{-1}. The X-ray photoelectron spectroscopy (XPS) data were collected with a monochromatic Al K_α source (1486.6 eV) at 100 W, 15 kV, and 6.7 mA using an X-ray photoelectron spectrometer (Thermo Fisher). The ion etching was performed by using Ar ions at 500 V and 1.7 μA. Raman spectra were acquired at 0.2 mW using a 532 nm Nd-YAG laser with Alpha300S (Witec Instrument). The HRTEM images and ED pattern were obtained using JEM-2100F (JEOL) with 200 kV and 0.105 mA. The electronic conductivity of TiS_2 samples was obtained by a four-probe method using pellets formed at 130 MPa.[32]

Results and discussion

Lithiation of TiS_2 by reaction with Li_3N *via* the mechanochemical reaction is a safe, easy, and fast (2 h) process. Spontaneous lithiation of TiS_2 by reaction with Li_3N was confirmed from rough thermodynamic calculations by considering the oxidative decomposition potential of Li_3N ($6Li^+ + N_2 + 6e^- \rightarrow 2Li_3N$, 0.44 V *vs.* Li/Li^+) and the lithiation–delithiation potential of TiS_2 ($TiS_2 + Li^+ + e^- \rightarrow LiTiS_2$, ~2.1 V *vs.* Li/Li^+).[33] The mechanochemically lithiated TiS_2 was exfoliated by reaction with water under ultrasonication. The van der Waals interaction between the interlayers of TiS_2 is weakened after lithiation of TiS_2. Then, gaseous H_2 evolved by the reduction of H_2O by Li within the TiS_2 layers of lithiated TiS_2 (LTS) pushes apart the interlayers of TiS_2. The TiS_2 layers are then split by the external force derived from ultrasonication, eventually resulting in exfoliation.[23,24,31,34] The as-synthesized TiS_2 NSs in contact with the sulphide SE (LGPS) are evaluated as a cathode material in bulk-type ASLBs (Fig. 1).

Fig. 2a shows the XRD patterns of bulk TiS_2 (b-TiS_2), LTS, and TiS_2-NS. The main peak in the pattern of b-TiS_2 appears at 15.5°, corresponding to the (001) plane of TiS_2 (JCPDS no. 15-0853) along the *c*-axis. After the mechanochemical reaction with Li_3N, this peak shifts negatively (14.3°), reflecting an increase in the interlayer distance of TiS_2 due to the intercalation of the Li ions.[21] Compared to the sharp peak for b-TiS_2, the broadened peak for LTS indicates decreased crystallinity and/or grain size, which results from the high-energy ball-milling process. After exfoliation, a significantly broadened peak with a notably lowered intensity was apparent at 15.4°. Firstly, the almost identical position of the peak in the pattern of TiS_2-NS and b-TiS_2 reflects the removal of Li from LTS after exfoliation. The amount of remaining Li in TiS_2-NS appeared to be $x = \sim 0.1$ in Li_xTiS_2, which was obtained by analysing the capacities of TiS_2-NS/Li cells using a liquid electrolyte (Fig. S1, ESI†). Secondly, the weak and broadened peak of TiS_2-NS indicates a decrease in the degree of stacking of TiS_2 along the [001] direction, which agrees well with the results for other exfoliated TMD NSs.[23,24] Successful exfoliation to generate nanosheets was also confirmed by atomic force microscopy (AFM) (Fig. S2, ESI†); the thickness of the nanosheets corresponds to a few layers of TiS_2. The irregular morphologies of TiS_2-NS may result from the breaking and crumbling of the LTS powder during the high-energy mechanochemical lithiation process. This is supported by the broadened (001) peak with lowered intensity in the XRD pattern of LTS as compared to that of b-TiS_2 (Fig. 2a). The Raman spectra (Fig. 2b) of b-TiS_2 and TiS_2-NS both show the same peaks centered at 332 cm^{-1} and 233 cm^{-1}, which originate from the A_{1g} and E_g modes of TiS_2, respectively, indicating that the intra-layer structure of TiS_2 layers remained intact after exfoliation from b-TiS_2.[21,35]

The chemical states of TiS_2-NS were analysed by the acquisition of the Ti 2p XPS data (Fig. 2c). The b-TiS_2 sample shows two characteristic peaks of TiS_2 at 456.4 eV and 462.4 eV, which agree well with the previously reported data.[21] The TiS_2-NS sample shows peaks of TiS_2 as well as additional peaks at 459.0 eV and 464.5 eV. These peaks are assigned to TiO_2, indicating a partial oxidation of TiS_2-NS.[36] It is reported that TiS_2 can be oxidized by both O_2 and water, and the oxidation rate is faster during exposure to O_2 compared to water.[35] Even though exposure to gaseous O_2 was avoided during the preparation of TiS_2-NSs, contact with water was inevitable during exfoliation, resulting in the oxidation of TiS_2.[37] The TiO_2/TiS_2 atomic ratio was obtained by analyzing the deconvoluted signals of the TiO_2 and TiS_2 peaks. The TiO_2/TiS_2 atomic ratio obtained without ion-etching was approximately 1.4, which decreased to 0.6 after ion-etching for 80 s, indicating oxidation at the surface of TiS_2-NSs. Ti K-edge X-ray absorption near-edge structure (XANES) and extended X-ray absorption fine structure (EXAFS) spectra of TiS_2-NSs revealed that a major component of TiS_2-NSs is TiS_2 rather than TiO_2 (Fig. S3, ESI†). The fact that no other peaks except for those of TiS_2 are seen in the XRD pattern (Fig. 2a) indicates the presence of an amorphous TiO_2 layer on the surface of TiS_2-NSs. The high resolution transmission electron microscopy (HRTEM) image and the corresponding selected area electron diffraction (SAED) pattern of TiS_2-NSs presented in Fig. 2d reveal the microstructure of TiS_2-NSs. A few layered bundles were observed, corresponding to less-exfoliated

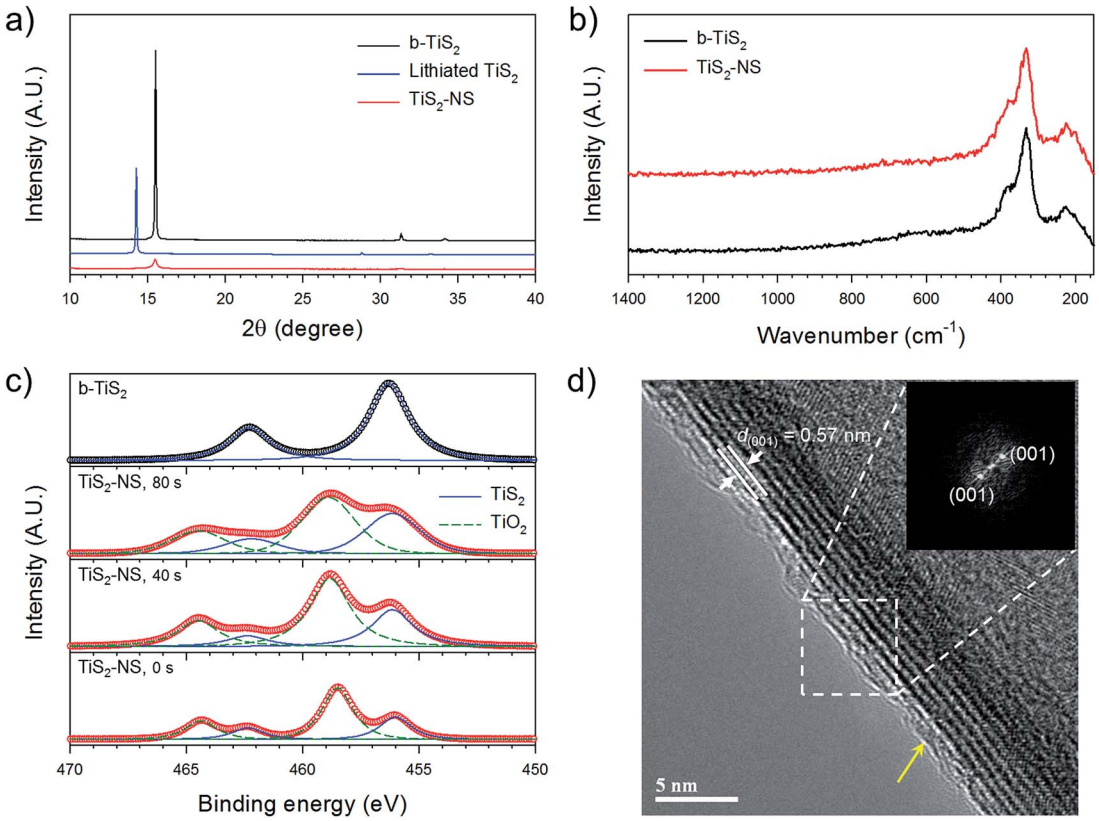

Fig. 2 Characterization of the TiS_2-NS. (a) XRD patterns of bulk-TiS_2 (b-TiS_2), lithiated TiS_2 (LTS), and the TiS_2-NS. (b) Raman spectra of b-TiS_2 and TiS_2-NS. (c) XPS spectra of b-TiS_2 and the TiS_2-NS. The ion-etching times are indicated for the TiS_2-NS. The XPS data were deconvoluted into signals from TiS_2 and TiO_2, which are represented by the solid and dashed lines, respectively. (d) HRTEM image and its corresponding ED pattern of the TiS_2-NS. The arrow indicates an amorphous layer.

or restacked TiS_2 layers. The interlayer distance (0.57 nm) and the SAED pattern correspond well to the (001) peak in the XRD pattern (Fig. 2a). The presence of a thin amorphous layer (indicated by the arrow) on the TiS_2 layers is also in line with the signature of TiO_2 from the XPS spectra (Fig. 2c). The scanning TEM image and its corresponding energy dispersive X-ray spectroscopy (EDXS) elemental map show the even distribution of Ti, S, and O over the TiS_2-NS particles, revealing a uniform and slight oxidation of the TiS_2-NS surfaces (Fig. S4, ESI†). In addition, the lower electronic conductivity of TiS_2-NSs (2.6 S cm^{-1}) compared to that of b-TiS_2 (3.1×10^2 S cm^{-1}) can be explained by the presence of a thin insulating TiO_2 layer covering the metallic TiS_2 layers. It should be noted that the conductivity of 2.6 S cm^{-1} is sufficiently high for battery application,[15,21] which is in sharp contrast to the low conductivities of other exfoliated TMD NSs.[23]

The TiS_2-NS sample was evaluated as a cathode material for bulk-type ASLBs using sulphide SEs. The configuration of the all-solid-state cell is depicted in Fig. 1. LGPS and Li_3PS_4 (LPS) with conductivities of 6.0×10^{-3} S cm^{-1} and 1.0×10^{-3} S cm^{-1} at 30 °C were employed as the SEs. The state-of-the-art SE, LGPS, used in the composite electrode layer and the LGPS/LPS bilayer can maximize the overall rate performance while retaining good interfacial stability at the Li–In anode.[3,10,15] The as-fabricated TiS_2/Li–In all-solid-state cells were cycled between 1.0 and 4.0 V (*vs.* Li/Li^+) at 50 mA g^{-1} (0.2C) at 30 °C. The weight ratio of TiS_2 : SE : Super P was 10 : 10 : 0.5 (the weight fraction of the SE was 48.8%). The second-cycle discharge (lithiation) and charge (delithiation) voltage profiles and their corresponding differential voltage profiles of b-TiS_2 and TiS_2-NS in the all-solid-state cells are shown in Fig. 3 and S5 (ESI†), respectively. The capacity values are based on the weight of TiS_2. The reversible capacities (charge capacities) of b-TiS_2 and TiS_2-NSs were 259 mA h g^{-1} and 277 mA h g^{-1}, respectively, which slightly exceed the theoretical capacity of TiS_2 ($TiS_2 + Li^+ + e^- \rightarrow LiTiS_2$, 239 mA h g^{-1}).

The lithiation (discharge) voltage ranges in the discharge voltage profiles can be divided into two regions, *i.e.*, higher (region I) and lower (region II) than 1.7 V (*vs.* Li/Li^+) (Fig. 3). In region I, the discharge capacity of the TiS_2-NS (~200 mA h g^{-1}) is lower than that of b-TiS_2 (~220 mA h g^{-1}). Considering that the sloping plateau at ~2.1 V in region I originates from the intercalation of Li ions into TiS_2,[15,21] the lower capacity in region I for the TiS_2-NS might reflect a slight loss of TiS_2 from the TiS_2-NS. This is in line with the observed partial oxidation of TiS_2-NSs, which is evidenced by the XPS (Fig. 2c), HRTEM (Fig. 2d), and electronic conductivity data. In contrast, the capacity in region II for the TiS_2-NS (~90 mA h g^{-1}, Fig. 3b) is much larger than that for b-TiS_2 (~40 mA h g^{-1}, Fig. 3a). Firstly, the amorphous TiO_2 layer in the TiS_2-NS could contribute to the capacity in region II. Amorphous TiO_2 can uptake Li ions over

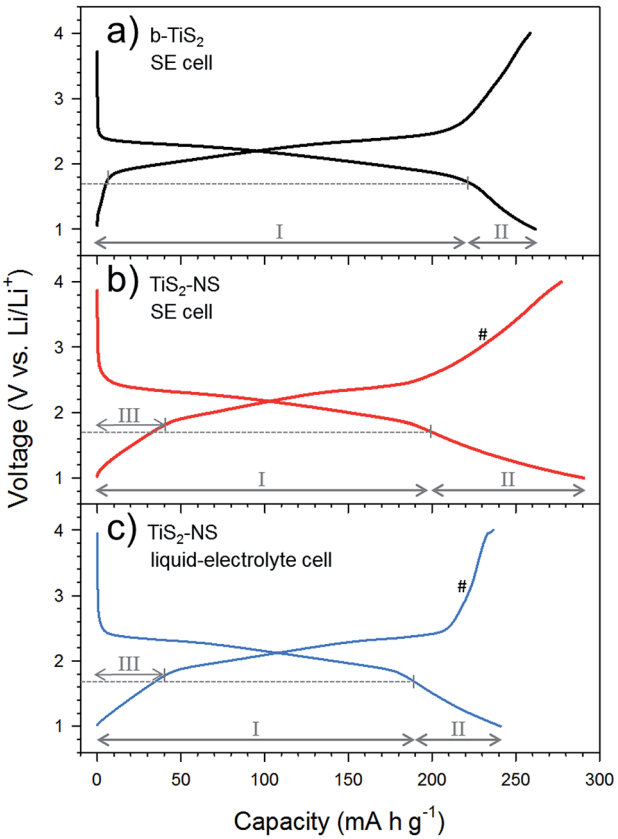

Fig. 3 Second-cycle discharge–charge voltage profiles of TiS_2/Li–In all-solid-state cells with (a) b-TiS_2 and (b) TiS_2-NS, and (c) for a TiS_2-NS/Li liquid-electrolyte cell. Regions I and II in the discharge (lithiation) voltage profiles are divided by 1.7 V (*vs.* Li/Li^+). Region III indicates the range in the charge process (delithiation) up to 1.8 V (*vs.* Li/Li^+). The sloping voltage region denoted as '#' is explained in the main text.

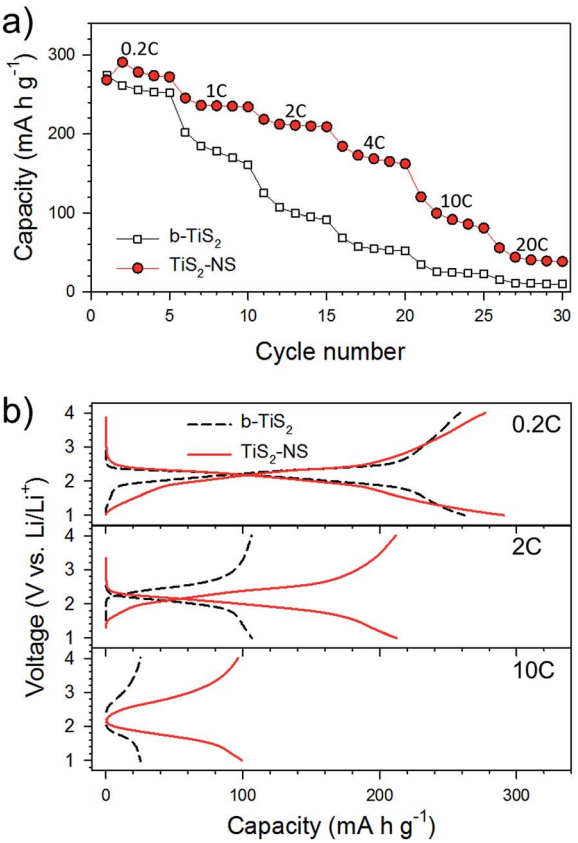

Fig. 4 Rate performance of TiS_2/Li–In all-solid-state cells with b-TiS_2 and the TiS_2-NS. (a) Discharge capacity varied by C-rates as a function of the cycle number and (b) its corresponding discharge–charge voltage profiles at different C-rates.

a wide voltage range of 1.0–2.5 V (*vs.* Li/Li^+) in the sloping voltage curve.[38,39] Secondly, because of the much larger contact area between the TiS_2-NS and the SE (LGPS) than that between b-TiS_2 and the SE, the partial participation of the SE in the reversible lithiation–delithiation process at the TiS_2-SE interfaces can be maximized for the TiS_2-NS. A reversible capacity of >100 mA h $(g \text{ of the SE})^{-1}$ was reportedly achieved by tailoring active-material-free composite electrodes.[40,41] In order to estimate the contribution of the SE (LGPS) to the capacity in region II, the second discharge–charge voltage profiles and their corresponding differential voltage profiles for the liquid-electrolyte cell with the TiS_2-NS are compared in Fig. 3c and S5c (ESI†). While the capacities of the all-solid-state cell and liquid-electrolyte cell are almost the same in region I, the capacity of the liquid-electrolyte cell in region II (~50 mA h g^{-1}, Fig. 3c) is much lower than that of the all-solid-state cell (~90 mA h g^{-1}, Fig. 3b), which adequately supports the appreciable participation of LGPS in contact with the TiS_2-NS in the reversible reaction with Li.

In the charge (delithiation) voltage profiles, there is a noticeable variation of the capacity in the sloping voltage region up to ~1.8 V (*vs.* Li/Li^+) (region III). The capacity of the TiS_2-NS in region III was much larger than that of b-TiS_2 for the respective all-solid-state cells (Fig. 3a), which may be attributed to the appreciable contribution of TiO_2 and/or the SE in contact with the TiS_2-NS. Notably, the capacities of both all-solid-state (Fig. 3b) and liquid-electrolyte (Fig. 3c) TiS_2-NS cells in region III (~40 mA h g^{-1}) are almost identical and are also the same as the difference in the discharge capacities of the all-solid-state cell and liquid-electrolyte cells in region II (90 mA h g^{-1} (Fig. 3b) – 50 mA h g^{-1} (Fig. 3c)). It is thus reasonable to assign the capacity in region III to the contribution from TiO_2 mostly. In contrast, delithiation of the SE is thought to occur at higher voltages. In the sloping voltage region above ~2.5 V (*vs.* Li/Li^+) (denoted as '#'), the capacity of the all-solid-state cell (Fig. 3b) is significantly larger than that of the liquid-electrolyte cell (Fig. 3c). This reflects the contribution of the SE at high voltage and is consistent with the previous results for the pure LPS and LGPS electrodes.[40,41]

Capacities in all-solid-state cells with a higher weight fraction of SEs in the composite electrode layers (64.5 wt%, the weight ratio of TiS_2 : SE : Super P was 10 : 20 : 1.) are also compared (Fig. S6, ESI†). By increasing the weight fraction of the SE in composite electrode layers, the reversible (charge) capacity of b-TiS_2 is increased from 259 mA h g^{-1} (48.8 wt% of the SE, Fig. 3a) to 289 mA h g^{-1} (64.5 wt% of the SE, Fig. S6a, ESI†). When it comes to the TiS_2-NS, the increase in reversible capacity is dramatic; from 277 mA h g^{-1} (48.8 wt% of the SE,

Fig. 3b) to 532 mA h g^{-1} (64.5 wt% of the SE, Fig. S6b, ESI†). This observation reflects the pronounced effect of intimate contacts between TiS_2 and the SE in the TiS_2-NS all-solid-state cells. This in turn supports the appreciable participation of the SE (LPGS) in reversible lithiation and delithiation processes for the TiS_2-NS-based all-solid-state cells.

The rate capabilities of all-solid-state cells with b-TiS_2 and the TiS_2-NS cycled between 1.0 and 4.0 V (*vs.* Li/Li^+) at 30 °C are compared in Fig. 4a and b. The weight ratio of TiS_2 : SE : Super P was 10 : 10 : 0.5. The rate performance of TiS_2-NS is clearly superior to that of b-TiS_2. The cell with the TiS_2-NS retained 59% of its capacity at 4C (173 mA h g^{-1}) with respect to the capacity at 0.2C (291 mA h g^{-1}) (Fig. 4a). In sharp contrast, the capacity retention for the cell with b-TiS_2 at 4C was only 22%. In addition, b-TiS_2 exhibits larger polarization than the TiS_2-NS in the discharge–charge voltage profiles (Fig. 4b). The excellent rate performance of the TiS_2-NS is attributed to its unique 2D morphology and maintenance of the high electronic conductivity. The ultrathin 2D structure offers a short Li-ion diffusion path length and high interfacial contact area with the SE, rendering net movement of the Li ions across the interfaces a facile process.[3,42,43] For comparison, decreasing the size of TiS_2 particles was also attempted by conventional high-energy ball-milling (BM). The electrochemical behaviour of BM-TiS_2 is summarized in Fig. S7 and S8 (ESI†). The BM-TiS_2 cell also exhibited enhanced rate capability compared to the b-TiS_2 cell. However, the improvement achieved with BM is not as dramatic as that achieved with exfoliation (TiS_2-NS), which highlights the effectiveness of exfoliation for dimensional control.

The cycling performances of all-solid-state cells with b-TiS_2 and TiS_2-NS cycled between 1.0 and 4.0 V (*vs.* Li/Li^+) at relatively high current density, 1C, are also compared in Fig. 5. The capacity retention of b-TiS_2 at the 50th cycle is 68.5%, which is sharply contrasted by 98.7% for the TiS_2-NS. The much better cycling performance of the TiS_2-NS than that of b-TiS_2 can be explained by relieved stress in volume change upon repeated discharge–charge cycling[32] and/or protective role of the amorphous oxide layers on the TiS_2 NS, which can alleviate the irreversible oxidation reaction of SEs.[13,18]

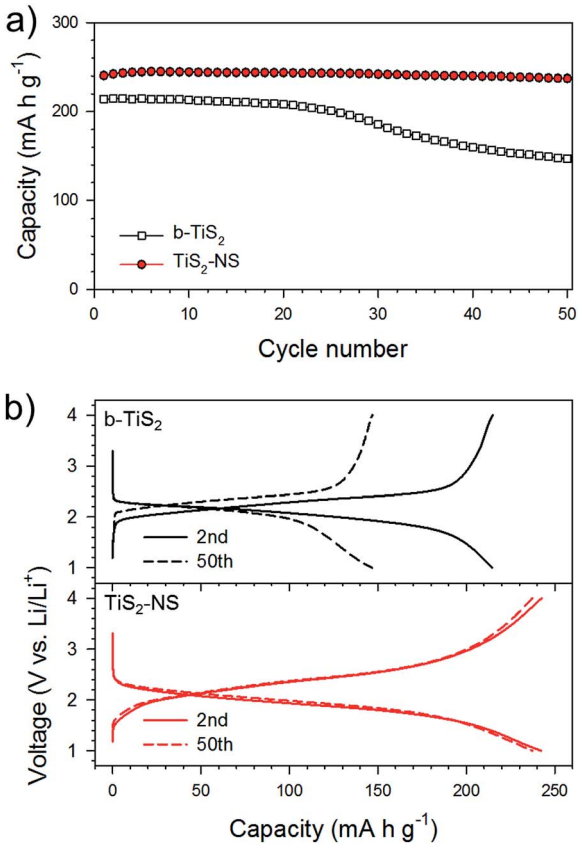

Fig. 5 Cycling performance of TiS_2/Li–In all-solid-state cells with b-TiS_2 and the TiS_2-NS. (a) Discharge capacity as a function of cycle number at 1C and (b) its corresponding discharge–charge voltage profiles at the 2nd and 50th cycles.

Conclusions

In summary, we successfully demonstrated the excellent electrochemical performance of sulphide-SE-based bulk-type ASLBs employing TiS_2 NSs prepared by scalable mechanochemical lithiation, followed by exfoliation in water under ultra-sonication. The enhancement of the reversible capacity was attributed to the SE region in intimate contact with the TiS_2-NS. The exceptionally superior rate capability of the TiS_2-NS compared to that of b-TiS_2 and BM-TiS_2, which is derived from the ultrathin 2D structure (the short Li ion diffusion length and the intimate contacts between the TiS_2-NS and the SE) and high electronic conductivity, was highlighted. The results of this study are not only important for the development of ASLB technology but also shed light on promising opportunities to further explore 2D nanomaterials for battery applications.

Acknowledgements

This work was supported by the Basic Science Research Program through the National Research Foundation of Korea (NRF) funded by the Ministry of Education (No. NRF-2014R1A1A2058760) and by the Energy Efficiency & Resources Core Technology Program of the Korea Institute of Energy Technology Evaluation and Planning (KETEP) grant funded by the Korea government Ministry of Trade, Industry & Energy (No. 20152010103470). Experiments at PLS were supported in part by MSIP and POSTECH.

Notes and references

1 N. Kamaya, K. Homma, Y. Yamakawa, M. Hirayama, R. Kanno, M. Yonemura, T. Kamiyama, Y. Kato, S. Hama, K. Kawamoto and A. Mitsui, *Nat. Mater.*, 2011, **10**, 682–686.
2 A. Hayashi, K. Noi, A. Sakuda and M. Tatsumisago, *Nat. Commun.*, 2012, **3**, 856.
3 K. H. Park, D. Y. Oh, Y. E. Choi, Y. J. Nam, L. Han, J.-Y. Kim, H. Xin, F. Lin, S. M. Oh and Y. S. Jung, *Adv. Mater.*, 2016, **28**, 1874–1883.
4 T. A. Yersak, H. A. Macpherson, S. C. Kim, V.-D. Le, C. S. Kang, S.-B. Son, Y.-H. Kim, J. E. Trevey, K. H. Oh, C. Stoldt and S.-H. Lee, *Adv. Energy Mater.*, 2013, **3**, 120–127.

5 Z. Lin, Z. Liu, W. Fu, N. J. Dudney and C. Liang, *Angew. Chem., Int. Ed.*, 2013, **52**, 7460–7463.
6 Y. S. Jung, D. Y. Oh, Y. J. Nam and K. H. Park, *Isr. J. Chem.*, 2015, **55**, 472–485.
7 Y. Seino, T. Ota, K. Takada, A. Hayashi and M. Tatsumisago, *Energy Environ. Sci.*, 2014, **7**, 627–631.
8 K. Xu, *Chem. Rev.*, 2004, **104**, 4303–4418.
9 A. Sakuda, A. Hayashi and M. Tatsumisago, *Sci. Rep.*, 2013, **3**, 2261.
10 Y. J. Nam, S.-J. Cho, D. Y. Oh, J.-M. Lim, S. Y. Kim, J. H. Song, Y.-G. Lee, S.-Y. Lee and Y. S. Jung, *Nano Lett.*, 2015, **15**, 3317–3323.
11 K. H. Kim, Y. Iriyama, K. Yamamoto, S. Kumazaki, T. Asaka, K. Tanabe, C. A. J. Fisher, T. Hirayama, R. Murugan and Z. Ogumi, *J. Power Sources*, 2011, **196**, 764–767.
12 S. Ohta, J. Seki, Y. Yagi, Y. Kihira, T. Tani and T. Asaoka, *J. Power Sources*, 2014, **265**, 40–44.
13 N. Ohta, K. Takada, L. Zhang, R. Ma, M. Osada and T. Sasaki, *Adv. Mater.*, 2006, **18**, 2226–2229.
14 F. Mizuno, A. Hayashi, K. Tadanaga, T. Minami and M. Tatsumisago, *Solid State Ionics*, 2004, **175**, 699–702.
15 B. R. Shin, Y. J. Nam, D. Y. Oh, D. H. Kim, J. W. Kim and Y. S. Jung, *Electrochim. Acta*, 2014, **146**, 395–402.
16 J. H. Woo, J. E. Trevey, A. S. Cavanagh, Y. S. Choi, S. C. Kim, S. M. George, K. H. Oh and S.-H. Lee, *J. Electrochem. Soc.*, 2012, **159**, A1120–A1124.
17 Y. Ito, Y. Sakurai, S. Yubuchi, A. Sakuda, A. Hayashi and M. Tatsumisago, *J. Electrochem. Soc.*, 2015, **162**, A1610–A1616.
18 A. Sakuda, A. Hayashi and M. Tatsumisago, *Chem. Mater.*, 2010, **22**, 949–956.
19 J. Haruyama, K. Sodeyama, L. Han, K. Takada and Y. Tateyama, *Chem. Mater.*, 2014, **26**, 4248–4255.
20 X. Xu, K. Takada, K. Fukuda, T. Ohnishi, K. Akatsuka, M. Osada, B. T. Hang, K. Kumagai, T. Sekiguchi and T. Sasaki, *Energy Environ. Sci.*, 2011, **4**, 3509–3512.
21 B. R. Shin, Y. J. Nam, J. W. Kim, Y.-G. Lee and Y. S. Jung, *Sci. Rep.*, 2014, **4**, 5572.
22 B. R. Shin and Y. S. Jung, *J. Electrochem. Soc.*, 2014, **161**, A154–A159.
23 M. Chhowalla, H. S. Shin, G. Eda, L.-J. Li, K. P. Loh and H. Zhang, *Nat. Chem.*, 2013, **5**, 263–275.
24 X. Huang, Z. Zeng and H. Zhang, *Chem. Soc. Rev.*, 2013, **42**, 1934–1946.
25 J. Xiao, D. Choi, L. Cosimbescu, P. Koech, J. Liu and J. P. Lemmon, *Chem. Mater.*, 2010, **22**, 4522–4524.
26 Y. Liang, R. Feng, S. Yang, H. Ma, J. Liang and J. Chen, *Adv. Mater.*, 2011, **23**, 640.
27 K. Chang and W. Chen, *ACS Nano*, 2011, **5**, 4720–4728.
28 T. A. Yersak, J. E. Trevey and S.-H. Lee, *J. Power Sources*, 2011, **196**, 9830–9834.
29 P. Joensen, R. F. Frindt and S. R. Morrison, *Mater. Res. Bull.*, 1986, **21**, 457–461.
30 Z. Zeng, Z. Yin, X. Huang, H. Li, Q. He, G. Lu, F. Boey and H. Zhang, *Angew. Chem., Int. Ed.*, 2011, **50**, 11093–11097.
31 Z. Zeng, T. Sun, J. Zhu, X. Huang, Z. Yin, G. Lu, Z. Fan, Q. Yan, H. H. Hng and H. Zhang, *Angew. Chem., Int. Ed.*, 2012, **51**, 9052–9056.
32 Y. S. Jung, K. T. Lee, J. H. Ryu, D. Im and S. M. Oh, *J. Electrochem. Soc.*, 2005, **152**, A1452–A1457.
33 A. Rabenau, *Solid State Ionics*, 1982, **6**, 277–293.
34 C. N. R. Rao, H. S. S. R. Matte and U. Maitra, *Angew. Chem., Int. Ed.*, 2013, **52**, 13162–13185.
35 S. J. Sandoval, X. K. Chen and J. C. Irwin, *Phys. Rev. B: Condens. Matter Mater. Phys.*, 1992, **45**, 14347–14353.
36 S. Södergren, H. Siegbahn, H. Rensmo, H. Lindström, A. Hagfeldt and S.-E. Lindquist, *J. Phys. Chem. B*, 1997, **101**, 3087–3090.
37 J. H. Han, S. Lee, D. Yoo, J.-H. Lee, S. Jeong, J.-G. Kim and J. Cheon, *J. Am. Chem. Soc.*, 2013, **135**, 3736–3739.
38 M. Hibino, K. Abe, M. Mochizuki and M. Miyayama, *J. Power Sources*, 2004, **126**, 139–143.
39 W. J. H. Borghols, D. Lützenkirchen-Hecht, U. Haake, W. Chan, U. Lafont, E. M. Kelder, E. R. H. van Eck, A. P. M. Kentgens, F. M. Mulder and M. Wagemaker, *J. Electrochem. Soc.*, 2010, **157**, A582–A588.
40 T. Hakari, M. Nagao, A. Hayashi and M. Tatsumisago, *J. Power Sources*, 2015, **293**, 721–725.
41 F. Han, T. Gao, Y. Zhu, K. J. Gaskell and C. Wang, *Adv. Mater.*, 2015, **27**, 3473–3483.
42 I. D. Scott, Y. S. Jung, A. S. Cavanagh, Y. Yan, A. C. Dillon, S. M. George and S.-H. Lee, *Nano Lett.*, 2011, **11**, 414–418.
43 D. Y. Oh, Y. J. Nam, K. H. Park, S. H. Jung, S.-J. Cho, Y. K. Kim, Y.-G. Lee, S.-Y. Lee and Y. S. Jung, *Adv. Energy Mater.*, 2015, **5**, 1500865.